



DØnote 4757-CONF

Measurement of the Drell-Yan Differential Cross Section and Forward-Backward Asymmetry in $p\bar{p} \rightarrow e^+e^-$ Events at $\sqrt{s} = 1.96$ TeV using the DØ Detector

The DØ Collaboration
URL <http://www-d0.fnal.gov>
(Dated: March 10, 2005)

We present measurements of the inclusive Drell-Yan e^+e^- differential cross section ($d\sigma/dM_{e^+e^-}$) and forward-backward asymmetry (A_{FB}) as a function of the dielectron invariant mass over the range $70 - 400$ GeV/ c^2 . The data sample consists of 177.3 pb $^{-1}$ of $p\bar{p}$ collisions at $\sqrt{s} = 1.96$ TeV collected by the DØ detector.

Preliminary Results for Winter 2005 Conferences

I. INTRODUCTION

The Drell-Yan process describes the annihilation of a quark-antiquark pair and the production of a dilepton pair via an intermediate Z -boson or virtual photon [1]. In this analysis we study the e^+e^- final state: $p\bar{p} \rightarrow \gamma^*/Z \rightarrow e^+e^-$. The presence of both vector and axial-vector couplings of the quarks and leptons to the Z -boson gives rise to an asymmetry in the polar emission angle θ of the electron in the rest frame of the e^+e^- pair. The differential cross section for the parton level process $q\bar{q} \rightarrow \gamma^*/Z \rightarrow e^+e^-$ can be written

$$\frac{d\sigma}{d(\cos \theta)} = A(1 + \cos^2 \theta) + B \cos \theta \quad (1)$$

The weak interaction introduces the asymmetry ($B \neq 0$), and A and B are functions that depend on the weak isospin and charge of the incoming quarks and the e^+e^- invariant mass. To minimize the effect of the unknown transverse momenta of the incoming quarks we measure the electron polar angle in the Collins-Soper reference frame [2]. The particle four-vectors are transformed to the e^+e^- rest frame and the polar angle θ^* is measured with respect to the z -axis, defined as the bisector of the proton beam momentum vector and the negative antiproton beam momentum vector.

The forward-backward asymmetry A_{FB} is defined by

$$A_{FB} = \frac{\sigma_F - \sigma_B}{\sigma_F + \sigma_B} \quad (2)$$

where σ_F and σ_B are the forward and backward cross sections defined by

$$\sigma_F = \int_0^1 \frac{d\sigma}{d(\cos \theta^*)} d(\cos \theta^*) \quad (3)$$

$$\sigma_B = \int_{-1}^0 \frac{d\sigma}{d(\cos \theta^*)} d(\cos \theta^*) \quad (4)$$

The forward-backward asymmetry depends on the vector and axial-vector couplings of the quarks and leptons to the Z -boson and is therefore sensitive to the effective weak mixing angle $\sin^2 \theta_W$. The largest asymmetry occurs at center-of-mass energies of around 70 GeV and above 110 GeV. At the Z -pole the asymmetry is dominated by the couplings of the Z boson and arises from the interference of the vector and axial components of its coupling. At large invariant mass the asymmetry is dominated by γ^*/Z interference and is almost constant (≈ 0.6), independent of invariant mass. The Tevatron allows measurement of the forward-backward asymmetry at partonic center-of-mass energies above the center-of-mass energy of LEP II. This measurement can be used not only to confirm the standard model γ^*/Z interference which dominates in this region, but also to investigate possible new phenomena which may alter A_{FB} such as new neutral gauge bosons [3] or large extra dimensions [4].

II. THE DØ DETECTOR

The elements of the DØ detector [5] that are most important to this measurement are the tracking system and the electromagnetic calorimeter. The magnetic central-tracking system is comprised of a silicon microstrip tracker (SMT) and a central fiber tracker (CFT), both located within a 2 T superconducting solenoidal magnet. The SMT has $\approx 800,000$ individual strips, with typical pitch of $50 - 80 \mu\text{m}$, and a design optimized for tracking and vertexing capability at pseudorapidities of $|\eta| < 3$. The system has a six-barrel longitudinal structure, each with a set of four layers arranged axially around the beam pipe, and interspersed with 16 radial disks. The CFT has eight thin coaxial barrels, each supporting two doublets of overlapping scintillating fibers of 0.835 mm diameter, one doublet being parallel to the collision axis, and the other alternating by $\pm 3^\circ$ relative to the axis. Light signals are transferred via clear light fibers to solid-state photon counters (VLPC) that have $\approx 80\%$ quantum efficiency.

The calorimeter system is comprised of three liquid-argon/uranium calorimeters: a central section (CC) covering $|\eta|$ up to ≈ 1 , and two end calorimeters (EC) extending coverage to $|\eta| \approx 4$, all housed in separate cryostats [6]. In addition to the preshower detectors, scintillators between the CC and EC cryostats provide sampling of developing showers at $1.1 < |\eta| < 1.4$.

Luminosity is measured using plastic scintillator arrays located in front of the EC cryostats, covering $2.7 < |\eta| < 4.4$. The trigger and data acquisition systems are designed to accommodate the high luminosities of Run II. Based on preliminary information from tracking, calorimetry, and muon systems, the output of the first level of the trigger is used to limit the rate for accepted events to ≈ 1.5 kHz. At the next trigger stage, with more refined information, the

rate is reduced further to ≈ 800 Hz. These first two levels of triggering rely mainly on hardware and firmware. The third and final level of the trigger, with access to all the event information, uses software algorithms and a computing farm, and reduces the output rate to ≈ 50 Hz, which is written to tape.

III. DATA SELECTION

Data were collected between September 2002 and September 2003 and correspond to an integrated luminosity of $177.3 \pm 11.5 \text{ pb}^{-1}$. Events were required to pass a single electron trigger and preselection requirements of at least one electromagnetic cluster in the calorimeter with transverse energy greater than 15 GeV. In the final offline event selection we require two electron candidates in the central calorimeter with $|\eta| < 1.1$ and $E_T > 25$ GeV. Both electron candidates must have an electromagnetic shower in the calorimeter consistent with an electron. These requirements are based on the fraction of energy in the electromagnetic portion of the calorimeter, the absence of energy close to the core ($\Delta R < 0.2$) of the EM cluster, and a transverse and longitudinal shower shape consistent with Monte Carlo electrons simulated with GEANT [7]. In order to reduce the backgrounds from direct photon and multijet events, and to determine the charge from the track curvature, at least one of the electron candidates must have a track matched to the calorimeter cluster. The invariant mass of the two electrons is required to be greater than $70 \text{ GeV}/c^2$. A total of 5259 candidate pass the selection criteria.

IV. EFFICIENCIES

Efficiencies of the trigger, electron identification and track match requirements are derived from Z events in the data sample. We use the “tag-and-probe” method, where a tag electron must pass tight electron requirements and the probe electron must pass all the requirements except the one under study. The efficiency is then the fraction of probe electrons passing the requirement under study. We obtain an electron identification efficiency for Z events of $(92.75 \pm 0.54)\%$, and a track match efficiency of $(79.9 \pm 0.5)\%$. To determine the variation of the electron identification and track match efficiencies as a function of invariant mass of the e^+e^- pair we use a sample of PYTHIA Drell-Yan events with a GEANT simulation of the DØ detector. The efficiencies decrease below and above the Z peak region due to the effects of photon radiation (see Fig. 1).

To determine the event trigger efficiency as a function of mass we use the Monte Carlo Drell-Yan events combined with the p_T dependent single-electron trigger efficiency derived from data. The efficiency is constant over the invariant mass range of interest and is equal to $1.0000^{+0.0000}_{-0.0006}$.

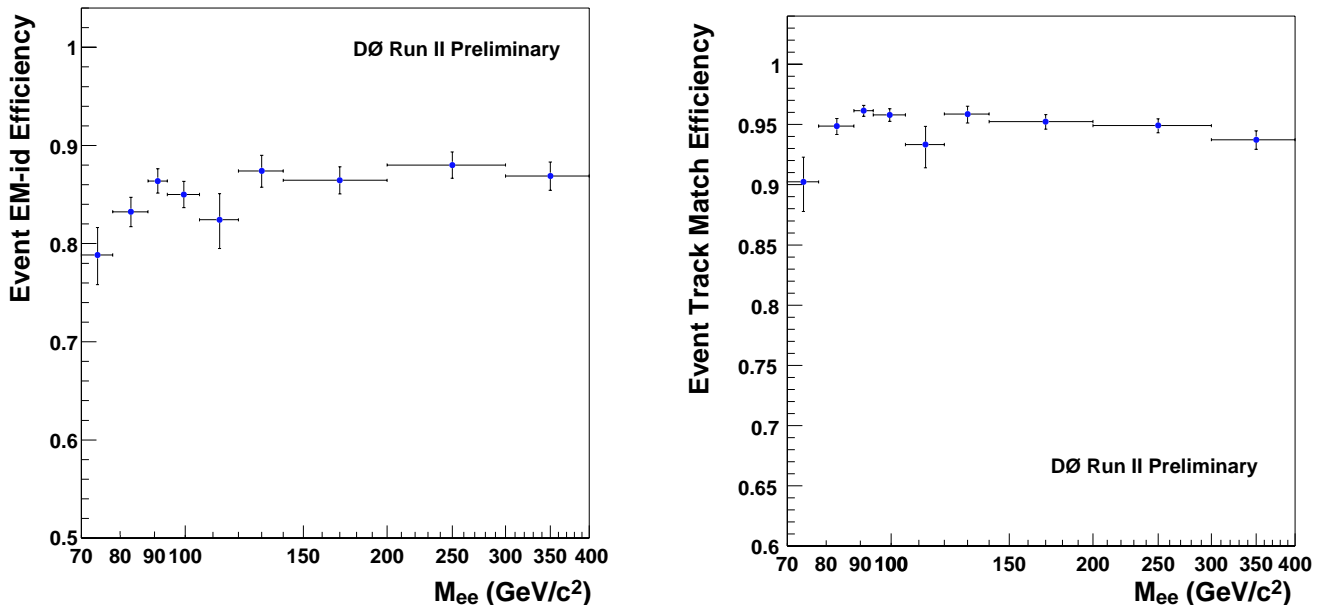


FIG. 1: Event EM-id efficiency (left) and event track match efficiency (right) as a function of e^+e^- invariant mass for all events. The efficiencies are normalized to data in the Z peak region.

V. BACKGROUND ESTIMATION

The main source of background for Drell-Yan e^+e^- events is the production of multijet and direct photon events, in which the jets have a large electromagnetic component (most of the energy is deposited in the EM section of the calorimeter) or they are mismeasured in some way that causes them to pass the electron selection criteria. This will be referred to as the QCD background. Other backgrounds are smaller and originate mainly from $W(\rightarrow e\nu) + \text{jets}$ events where a jet fakes an electron, $Z \rightarrow \tau^+\tau^-$, $W\gamma \rightarrow e\nu\gamma$, $WW \rightarrow e^+e^-$, and $t\bar{t} \rightarrow e^+e^-$.

The number of QCD background events is calculated by constructing two event samples: one passing all the signal event selection criteria described in the previous section (P events), and a parent sample of M events which passes the same requirements except that a track match is not required. Then the number of QCD background events is

$$N_{QCD} = \epsilon_b \left(\frac{\epsilon_s M - P}{\epsilon_s - \epsilon_b} \right) \quad (5)$$

where ϵ_s is the efficiency of the track match requirement for Drell-Yan signal events, and ϵ_b is the efficiency of the track match requirement for background events. The efficiency ϵ_s is calculated from the efficiency for a true electron in a signal event to have a track match (see Section IV). The efficiency ϵ_b is calculated from the probability that a fake electron from a jet in a QCD event has a track matched to it. This fake track match probability is determined using a sample of dijet events from data. The dijet events are required to be back-to-back and must have low missing transverse energy to remove $W \rightarrow e\nu + \text{jet}$ events. The jets must have at least five tracks within a cone of $\Delta R = 0.7$ to remove $Z \rightarrow \tau^+\tau^-$ events. In addition, one jet is required to pass standard jet requirements and the other jet must pass all the electron identification requirements (except for the track match). The fake probability is then the fraction of electron-like jets that have a matching track. The average fake probability is $(1.60 \pm 0.20)\%$.

The invariant mass distribution for the QCD background is determined from data. Events are required to pass all the signal selection criteria except that the EM calorimeter object must pass anti-quality shower shape cuts, i.e they must have a shower shape that is inconsistent with that of real electrons. This sample is composed predominantly of dijet events. The normalization of the background distribution is obtained from Eq. (5). The result for the estimated number of QCD background events is $N_{QCD} = 62.5 \pm 8.0$.

The background from $W(\rightarrow e\nu) + \text{jets}$ events is calculated from a Monte Carlo sample of $W(\rightarrow e\nu) + \text{jets}$ events. The events are weighted by the probability of a jet to fake an electron, obtained from a sample of dijet data events. The other backgrounds are calculated from Monte Carlo event samples. The total numbers of background events from each source are: 11.1 ± 3.4 from $W(\rightarrow e\nu) + \text{jets}$; 2.4 ± 1.8 from $Z \rightarrow \tau^+\tau^-$; 3.4 ± 1.9 from $W\gamma$; 1.6 ± 1.4 from WW ; and 1.5 ± 1.3 from $t\bar{t}$.

VI. MONTE CARLO SIMULATION

A parametrized Monte Carlo simulation (PMCS) of the DØ detector is used to determine corrections for kinematic acceptance, geometric acceptance, the effects of the detector resolution, and for the effects of QED radiation. The Drell-Yan events are generated using PYTHIA [8] over the invariant mass range 70–400 GeV/ c^2 . PHOTOS [9] is used to model the QED radiative corrections, and the events were generated with the CTEQ6M parton distribution functions [10]. Figure 2 compares the results of the simulation to the e^+e^- invariant mass distribution observed in the data.

VII. UNCORRECTED FORWARD-BACKWARD ASYMMETRY

In this section we compare the measured forward-backward asymmetry with predictions of the Monte Carlo simulation. The measured or “raw” asymmetry is defined by

$$A_{FB}^{raw} = \frac{(N_F - B_F) - (N_B - B_B)}{(N_F - B_F) + (N_B - B_B)} \quad (6)$$

where N_F, N_B are the observed number of forward and backward events in the data, and B_F, B_B are the estimated backgrounds for forward and backward events, respectively. The data are not corrected for kinematic acceptance, geometric acceptance, detector resolution, or QED radiation effects.

The raw forward-backward asymmetry from data is shown in Fig. 3, and is compared to the Monte Carlo prediction. Good agreement between the data and the standard model prediction is seen; the chi-square per degree of freedom is $\chi^2/\text{dof} = 1.47$.

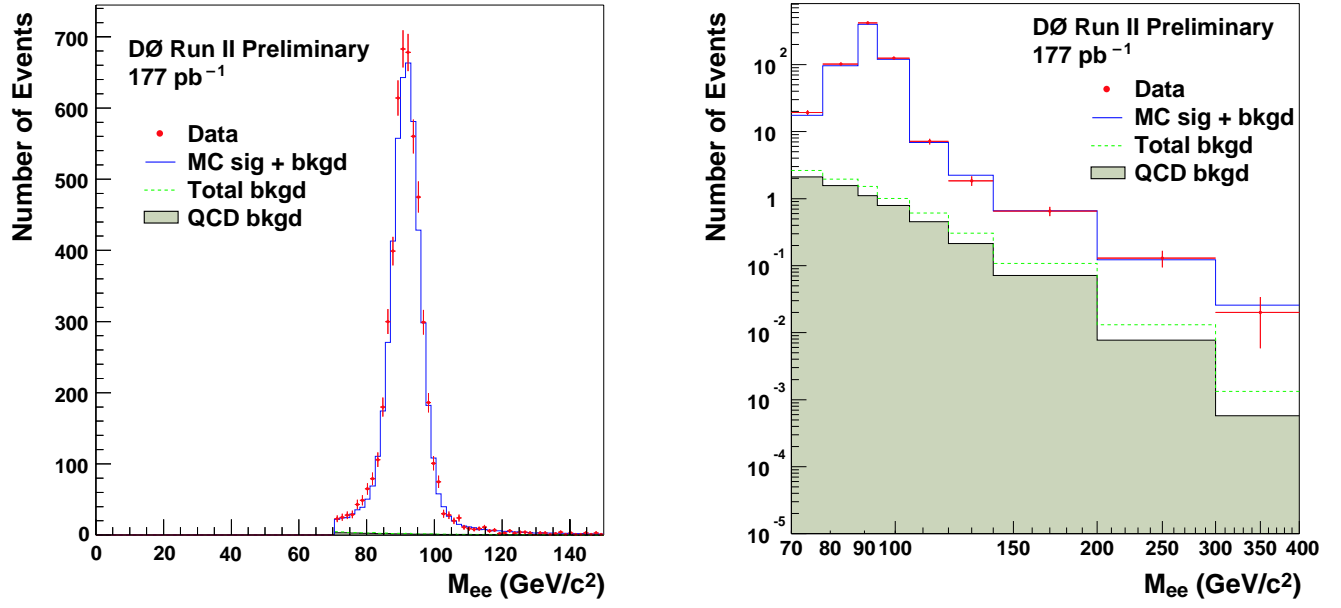


FIG. 2: Comparison of the e^+e^- invariant mass distribution from data with that from Monte Carlo with linear (left) and log (right) axis scales. The points are the data (showing the statistical errors only), the dashed line is the total background estimate, the shaded histogram is the QCD background, and the solid line is the sum of the signal Monte Carlo and the background estimate.

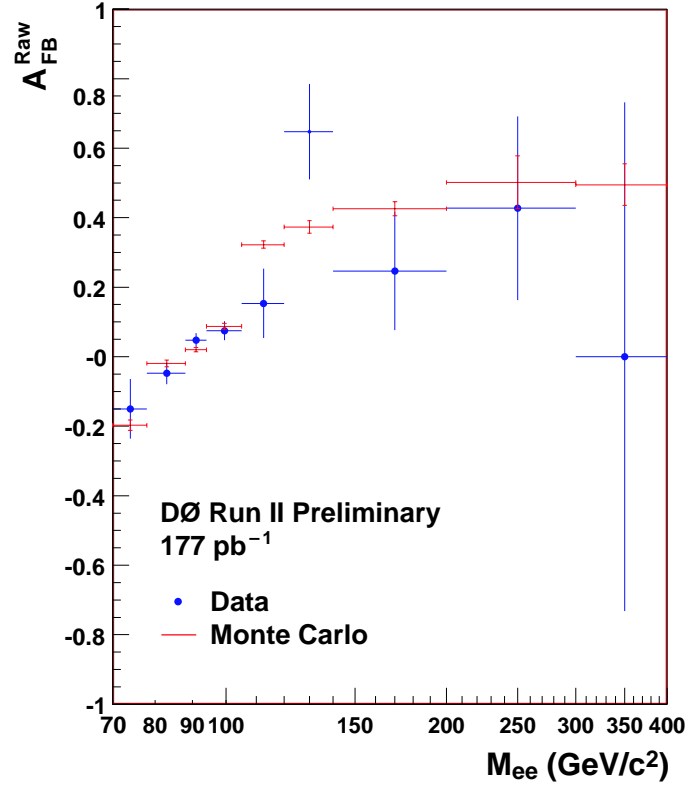


FIG. 3: Comparison of the raw forward-backward asymmetry distribution from data with the prediction of the Monte Carlo. The blue points are data with statistical errors only and the red line is the Drell-Yan Monte Carlo.

VIII. DRELL-YAN DIFFERENTIAL CROSS SECTION

An estimate of the “true” invariant mass distribution is computed correcting each bin i of the observed experimental distribution by the ratio of the “true” to the “observed” Monte Carlo event numbers:

$$d_i^{\text{true}} = \frac{m_i}{m'_i} \cdot d_i^{\text{obs}} \equiv \frac{d_i^{\text{obs}}}{\beta_i} \quad (7)$$

where the correction factor is $\beta_i = m'_i/m_i$, i.e. the ratio of the “observed” to the “true” Monte Carlo event numbers. We obtain m'_i from the number of Monte Carlo events passed through the PMCS detector simulation which pass the kinematic and acceptance cuts and have a reconstructed e^+e^- mass in bin i . Similarly, m_i is the number of Monte Carlo events generated with no QED radiation and with generator-level e^+e^- mass in bin i . Figure 4 shows the correction factors as a function of e^+e^- mass for forward and backward events. At large invariant mass the correction factor for forward events is lower than that for backward events since electrons in forward events have a wider $|\eta|$ distribution compared to backward events, and therefore have a lower efficiency of falling within the geometric acceptance of the central calorimeter.

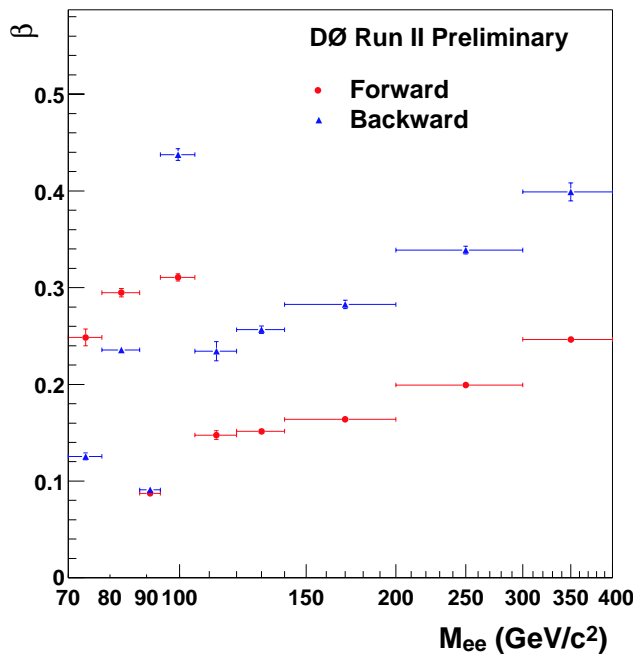


FIG. 4: Correction factor β for forward and backward events as a function of e^+e^- invariant mass. This factor corrects for kinematic acceptance, geometric acceptance, the effects of the detector resolution, and the effects of QED radiation.

The Drell-Yan differential cross section in each e^+e^- invariant mass bin is given by

$$\left(\frac{d\sigma}{dM} \right)_i = \frac{N_i - B_i}{\epsilon_i \beta_i \mathcal{L} \Delta M_i}, \quad (8)$$

where N_i is the number of observed events, B_i is the background estimate, ϵ_i is the total event selection efficiency, β_i is the correction factor for acceptance, detector resolution, and QED radiative corrections, \mathcal{L} is the integrated luminosity and ΔM_i is the bin width. Figure 5 shows the differential cross section and compares our results to the order α_s^2 calculation of Ref. [11]. The result for each mass bin, together with the statistical and systematic errors, are given in Table I.

The sources of systematic error arise from uncertainties in the background estimate, the efficiencies and the correction factor β . The overall uncertainty in β includes the uncertainties in the detector modeling, the transverse momentum of the e^+e^- system, and the parton distribution functions. There is also a systematic error on the cross section of 6.5% arising from the uncertainty in the integrated luminosity of the data sample. This relative uncertainty is the same for all bins and is not included in the error bars in Fig. 5.

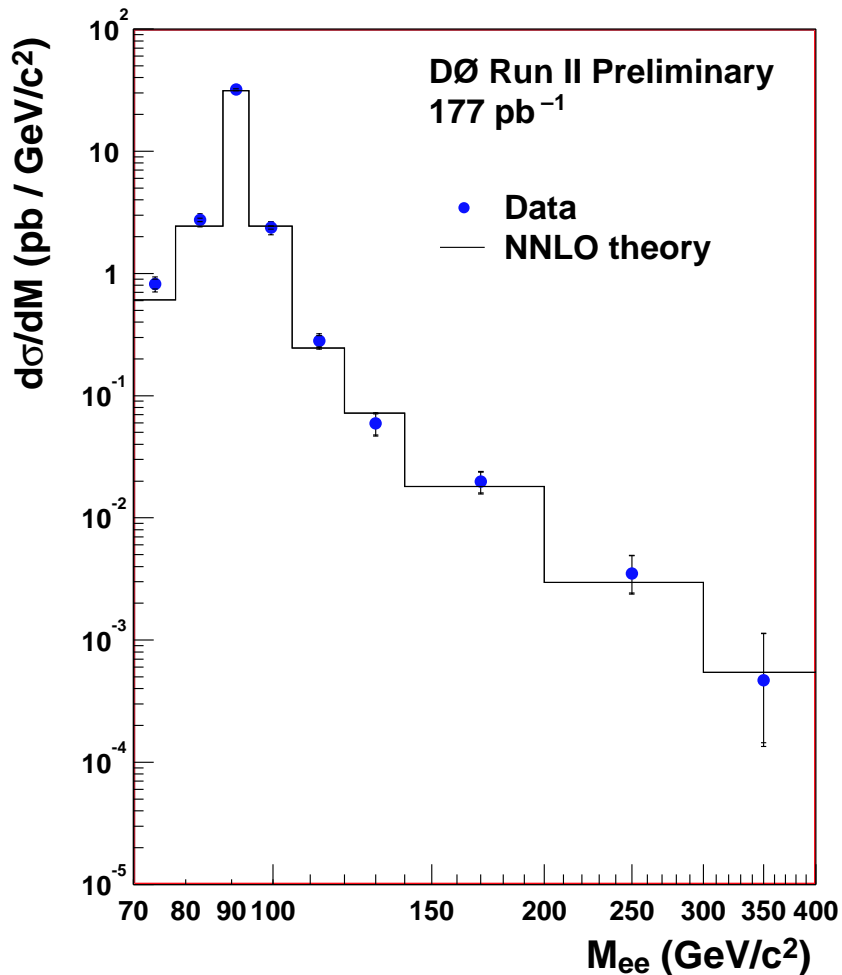


FIG. 5: The Drell-Yan differential cross section. The points with error bars are data with the error bars representing the total uncertainty (outer error bars) and the statistical uncertainty only (inner error bars). The systematic error of 6.5% due to the uncertainty in the integrated luminosity is not included in the error bars shown here. The histogram is a NNLO theoretical calculation [11].

IX. FORWARD-BACKWARD ASYMMETRY

The forward-backward asymmetry, corrected for kinematic acceptance, geometric acceptance, detector resolution, and QED radiation effects, is obtained by calculating the differential cross section for forward and backward events separately from Eq. (8), then using Eq. (2). The result is also corrected for the effects of charge mismeasurement. This correction is derived from the probability of incorrectly measuring the electron charge, which is obtained from the fraction of opposite sign events observed in the data in the Z -peak region. We obtain $P_m = 0.006 \pm 0.005$ for the charge mismeasurement probability. The variation of P_m with e^+e^- invariant mass is obtained from Monte Carlo events passed through the GEANT detector simulation. The probability rises at high invariant mass due to the electron tracks becoming almost straight; in the two highest mass bins we find $P_m \approx 0.06 - 0.07$.

Figure 6 shows the forward-backward asymmetry as a function of e^+e^- invariant mass. Also shown are the Born-level predictions from PYTHIA and ZGRAD [12]. Table I lists the results for each mass bin. The data are consistent with the standard model prediction over the entire mass range $70 - 400$ GeV/ c^2 covered by the measurements.

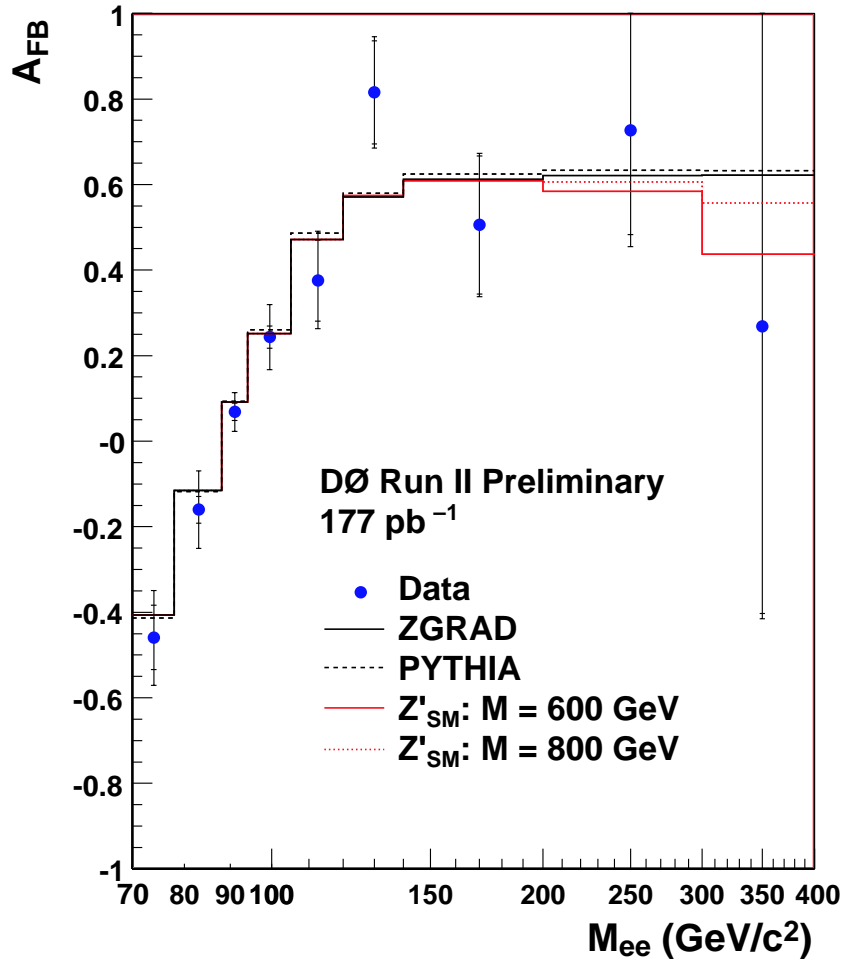


FIG. 6: Forward-backward asymmetry vs. dielectron invariant mass. The blue circles are the data with the error bars representing the total uncertainty (outer error bars) and the statistical uncertainty only (inner error bars). The black histograms are the Born-level theoretical calculation using PYTHIA (solid) and ZGRAD (dashed). The red histograms show the effect of adding a Z' with standard-model couplings to the theoretical prediction, including full $\gamma/Z/Z'$ interference. The predictions are shown for Z' masses of 600 and 800 GeV/c^2 . The width of the Z' was assumed to be 0.03 times the Z' mass.

TABLE I: Results of the measurements of the Drell-Yan differential cross section $d\sigma/dM_{e^+e^-}$ and forward-backward asymmetry A_{FB} for each e^+e^- invariant mass bin. There is an overall fractional uncertainty on $d\sigma/dM_{e^+e^-}$ of 6.5% from the uncertainty in the integrated luminosity. This is not included in the systematic errors listed in this table.

Mass Range (GeV/c^2)	$d\sigma/dM_{e^+e^-}$ ($\text{pb} / \text{GeV}/c^2$)	A_{FB}
70–78	0.821 ± 0.077 (stat.) $^{+0.070}_{-0.072}$ (syst.)	-0.459 ± 0.075 (stat.) $^{+0.080}_{-0.083}$ (syst.)
78–88	2.75 ± 0.09 (stat.) ± 0.27 (syst.)	-0.160 ± 0.031 (stat.) ± 0.085 (syst.)
88–94	31.9 ± 0.6 (stat.) ± 1.3 (syst.)	0.068 ± 0.020 (stat.) ± 0.040 (syst.)
94–105	2.37 ± 0.06 (stat.) ± 0.25 (syst.)	0.243 ± 0.026 (stat.) ± 0.072 (syst.)
105–120	0.281 ± 0.030 (stat.) $^{+0.023}_{-0.022}$ (syst.)	0.375 ± 0.095 (stat.) $^{+0.067}_{-0.060}$ (syst.)
120–140	0.0595 ± 0.012 (stat.) ± 0.004 (syst.)	0.82 ± 0.12 (stat.) ± 0.05 (syst.)
140–200	0.0199 ± 0.0038 (stat.) ± 0.0011 (syst.)	0.51 ± 0.16 (stat.) ± 0.04 (syst.)
200–300	$0.00350^{+0.0014}_{-0.0011}$ (stat.) ± 0.0003 (syst.)	$0.73^{+0.39}_{-0.24}$ (stat.) ± 0.12 (syst.)
300–400	$0.00047^{+0.00066}_{-0.00032}$ (stat.) ± 0.00008 (syst.)	$0.3^{+1.9}_{-0.7}$ (stat.) ± 0.1 (syst.)

Acknowledgments

We thank the staffs at Fermilab and collaborating institutions, and acknowledge support from the Department of Energy and National Science Foundation (USA), Commissariat à l’Energie Atomique and CNRS/Institut National de Physique Nucléaire et de Physique des Particules (France), Ministry of Education and Science, Agency for Atomic Energy and RF President Grants Program (Russia), CAPES, CNPq, FAPERJ, FAPESP and FUNDUNESP (Brazil), Departments of Atomic Energy and Science and Technology (India), Colciencias (Colombia), CONACyT (Mexico), KRF (Korea), CONICET and UBACyT (Argentina), The Foundation for Fundamental Research on Matter (The Netherlands), PPARC (United Kingdom), Ministry of Education (Czech Republic), Canada Research Chairs Program, CFI, Natural Sciences and Engineering Research Council and WestGrid Project (Canada), BMBF and DFG (Germany), Science Foundation Ireland, A.P. Sloan Foundation, Research Corporation, Texas Advanced Research Program, Alexander von Humboldt Foundation, and the Marie Curie Fellowships.

-
- [1] S.D. Drell and T.-M. Yan, Phys. Rev. Lett. **25**, 316 (1970); Erratum *ibid.* **25** 902 (1970)
 - [2] J.C. Collins and D.E. Soper, Phys. Rev. **D16**, 2219 (1977).
 - [3] F. Del Aguila, M. Quirós and F. Zwirner, Nucl. Phys. B **287**, 419 (1987); J. L. Rosner, Phys. Rev. D **35**, 2244 (1987); J. L. Rosner, Phys. Rev. D **54**, 1078 (1996).
 - [4] J. L. Hewett, Phys. Rev. Lett. **82**, 4765 (1999).
 - [5] DØ Collaboration, V. Abazov *et al.*, “The Upgraded DØ Detector”, in preparation for submission to Nucl. Instrum. Methods Phys. Res. A; T. LeCompte and H.T. Diehl, Ann. Rev. Nucl. Part. Sci. **50**, 71 (2000).
 - [6] DØ Collaboration, S. Abachi *et al.*, Nucl. Instrum. Methods Phys. Res. A **338**, 185 (1994).
 - [7] R. Brun *et al.*, CERN Program Library Writeup W5013 (1993).
 - [8] T. Sjöstrand, P. Eden, C. Friberg, L. Lonnblad, G. Miu, S. Mrenna, and E. Norrbin, Computer Physics Commun. **135**, 238 (2001).
 - [9] E. Barbiero and Z. Was, Comput. Phys. Commun. **79**, 291 (1994); E. Barbiero, B. van Eijk, and Z. Was, *ibid.* **66**, 115 (1991).
 - [10] J. Pumplin, D.R. Stump, J. Huston, H.L. Lai, P. Nadolsky, and W.K. Tung, J. High Energy Phys. JHEP07, 012 (2002).
 - [11] R. Hamberg, W.L. van Neerven, and T. Matsuura, Nucl. Phys. B **359**, 343 (1991); W. L. Van Neerven and E. B. Zijlstra, Nucl. Phys. B **382**, 11 (1992).
 - [12] U. Baur, S. Keller, and W.K. Sakumoto, Phys. Rev. D **57**, 199 (1998).